University of Warsaw

Faculty of Physics

Wiktor Krokosz

Student no. 406312

Towards a continuous wideband mmWave-to-optical converter based on room-temperature Rydberg atoms

Master's thesis in PHYSICS

Supervisors: dr hab. Michał Parniak-Niedojadło dr Mateusz Mazelanik University of Warsaw

Abstract

This thesis builds upon an established design for a microwave-to-optical converter, exploring the modifications needed to extend its functionality to the millimeter-wave (mmWave) regime. The primary challenge was engineering a precise and tunable narrow-band source to accurately characterize the conversion process. Two approaches were investigated: using an automotive radar and a photomixer. Although the radar enabled successful and efficient conversion, the data diverged from the theoretical model due to strong frequency sideband noise. Implementing technical adjustments proved to be complex enough to shift towards constructing a photomixer. Subsequently, the obtained results are discussed and compared to the theoretical model, analyzing the conversion via electromagnetically induced transparency and Autler-Townes splitting measurements. In addition, the thesis explores the conversion of thermal radiation as well as technical obstacles that appear in mmWave synthesis and manipulation.

Keywords

quantum optics, quantum metrology, Rydberg atoms, mmWave photonics

Tytuł pracy w języku polskim

Ciągły szerokopasmowy konwerter fal milimetrowych na fale optyczne oparty na atomach Rydberga w temperaturze pokojowej

Contents

Int	rodu	iction		4
1.	Elec	tronic	source preparations	7
	1.1.	PCB a	ssembly	7
			Radar selection	7
			Phase-locked loop	8
			Frequency locking tests	Ć
	1.2.		-Townes splitting	10
			ng experimental setup	12
	1.4.		c vapor test	12
	1.5.		ating the frequency spurs	13
2.	Initi	al mea	asurements	16
			rsion measurements	16
		2.1.1.	Conversion setup process	16
			Bandwidth and autocorrelation	17
	2.2.		rsion of thermal radiation	18
		2.2.1.	Derivation	18
		2.2.2.	Measurements	19
		2.2.3.	Attenuator	20
3.	Veri	ficatio	n using a photomixer	24
٠.			ole of operation	24
		_	test	25
			-Drever-Hall technique	26
	3.4.		bly of a frequency stabilizer	28
	0.1.		Cavity setup	28
			Optical setup	29
			Electronic setup	31
	3.5.		ridth and autocorrelation verification	31
	3.6.		etrization	33
			ed improvements	33
	9.1.		Parabolic mirror	34
			Metamaterials	34
			New electronic design	34
		5.1.5.	New electronic design	94
Su	mma	ry		36
ъ	c			0.0

Introduction

Millimeter waves (mmWaves), or extremely high frequencies (EHF), span the 30 to 300 GHz frequency band, correlating to wavelengths of 1-10 mm. Their significance has increased rapidly with the advent of 5G telecommunications and the escalating demands for enhanced wireless data transmission capabilities. Distinguished from microwaves or centimeter waves by their higher bandwidth, mmWaves facilitate technologies reliant on substantial data exchange, including automotive vehicles, drones, intersatellite communication, and advanced industrial machinery. In addition, shorter wavelengths enable the development of smaller antennas and ancillary equipment compared to traditional microwave technologies, promising more directed signals and improved frequency reuse. The mmWave band is also instrumental in radio astronomy, employed in satellite sensors and terrestrial telescope arrays situated at high altitudes.

However, mmWaves face challenges because of their high attenuation, which limits their range and necessitates the creation of highly sensitive detectors. This thesis builds upon an established experimental framework of microwave-to-optical conversion by S. Borówka et al. [1], adapting it for mmWaves. The demonstrated conversion is pivotal for linking superconducting qubits in quantum computers via fiber optics, offering a reliable, low-noise data transmission method. Such advancements herald the possibility of distributed quantum computing, underscoring the ongoing efforts to develop mmWave-based networks [2, 3].

The methodology of S. Borówka et al. [1] surpasses alternative microwave conversion techniques by enabling continuous operation at room temperature, with notable efficiency and bandwidth. This is achieved through the exploitation of alkali metal Rydberg atoms, which are defined as atoms whose single valence electron occupies a high-energy state. Over the last decades they have attracted considerable attention in the field of optics, as this configuration results in impressive characteristics. Their atomic radii can reach micrometers in scale, with lifespans reaching several milliseconds in magnetooptic traps [4]. The latter has been achieved for a state with maximal orbital momentum, while higher momentum states in general, can be described using the classical Bohr model of an atom.

This means that the energy levels can be derived from the Rydberg formula, scaling with the principal quantum number n as $\sim n^{-2}$. Each subsequent transition pair is increasingly densely packed, and as can be seen in Fig. 1a, they encompass the electromagnetic spectrum from the THz band down to radio frequencies. What is crucial for optics is that these transitions have large dipole moments, which means that they are very sensitive to external fields driving these transitions. Strong light-matter interactions make Rydberg atoms a great candidate for efficient and sensitive sensors and especially for a transducer binding different energy domains.

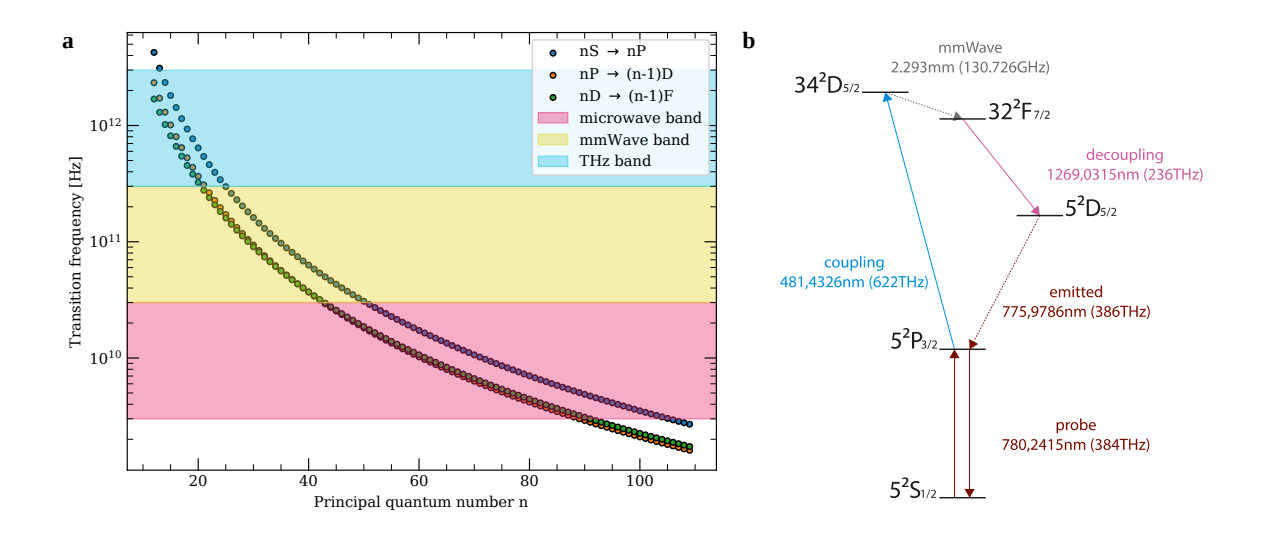


Figure 1: Subfigure a) depicts transition frequencies between subsequent energy levels for three selected transition families in Rubidium 85, spanning the entire micro- and mmWave bands, differentiated by colors. The THz band is also covered, but less densely. Subfigure b) qualitatively illustrates the energy levels involved in the underlying parametric process of the conversion mechanism.

Photon conversion in this study is facilitated through a parametric process, as depicted in Fig. 1. This is an extension of the typical Rydberg atom-based electric field sensor technique, which relies on a two-photon Rydberg excitation scheme. Measurement of the Autler-Townes (A-T) splitting of electromagnetically induced transparency (EIT) has been utilized with great success in electrometry and atomic receivers [5, 6, 7]. Two electromagnetic fields are required to operate. The probe field is used to obtain the absorption spectrum of the atomic vapor. The coupling field excites the atomic population into a high-energy Rydberg state, simultaneously inducing EIT. The introduction of an additional electric field leads to the A-T splitting, depending on this subsequent field. In this case, it facilitates a transition between two Rydberg states, which can be tuned to occur at a frequency in the mmWave band. Measurements of A-T splitting can provide accurate information about field intensity, phase [8], or frequency [9, 10]. The aforementioned extension involves the incorporation of a decoupling laser, which transfers the atomic population from the high-energy state, enabling the emission of photons in the optical band. All the driving fields in this setup are optical with convenient wavelengths. Additionally, very subtle tuning is required to move between the microwave and mmWave band. Consequently, minimal adjustments, primarily tuning of laser frequencies, were required for the existing setup. The main challenge involved designing an mmWave source with a sufficiently narrow bandwidth and controllable intensity to accurately characterize the converter parameters. Due to the unavailability of such devices commercially, it was imperative to construct the required equipment in-house.

While the EHF band is considered in most nomenclatures as part of the microwave spectrum, its high energies make it incompatible with most of the equipment utilized with typical RF fields. To highlight this distinction, the term microwaves refers to lower-energy frequencies, i.e. below 30 GHz. The mmWave band is also considered a part of the THz regime and as such belongs to the infamous THz gap, where both electronic and optical tooling reaches its technical limits. The issues of synthesis, field manipulation and detection present

numerous obstacles and considerable amount of research is going into overcoming them. The promising results of microwave sensing using Rydberg atoms, yields a promise of developing efficient sensors for this band as well. While electrometry using A-T splitting measurement has already been demonstrated [11, 12], but creating a transducer would open the door to even more applications and precise measurements, such as single photon counting.

In contrast to the generation of RF signals from lower-energy bands, synthesis of mmWaves using traditional electronics presents notable challenges. The compact size and high frequency associated with mmWaves enhance their susceptibility to numerous parasitic effects, leading to significant signal loss and thus compromising both precision and stability. On the other hand, most optical methods depend on nonlinear processes and are typically optimized for pulse operations, an exception is photomixing, which utilizes two stable laser sources to achieve frequency subtraction in continuous wave operation. This thesis provides a thorough investigation of both approaches and offers a detailed examination of the underlying engineering principles.

Chapter 1

Electronic source preparations

Compared to the well-established realm of microwave frequencies, where a plethora of off-the-shelf electronic devices are readily available, the landscape of mmWave technology presents unique challenges. Although modern signal generators excel in providing reliable performance across a wide range of frequencies, their capabilities often falter when it comes to reaching the mmWave spectrum. This deficiency stems from the inherent limitations of traditional electronic components and circuits, which struggle to operate efficiently at such high frequencies, resulting in a scarcity of commercially accessible solutions for generating mmWave signals.

Despite the shortcomings of commercial offerings, recent advancements in semiconductor technology have paved the way for on-chip synthesizers and transceivers capable of operating at mmWave frequencies. These integrated solutions offer a compact and cost-effective alternative to traditional equipment by leveraging the small wavelength of mmWave signals.

In the following sections, the methodology employed to overcome the challenges associated with generating mmWave frequencies is elucidated. This involves leveraging both existing commercial technologies and on-chip solutions. Through meticulous design and precise implementation, the aim is to construct a robust mmWave signal source that satisfies the stringent requirements of the experimental setup. This foundational work sets the stage for deepening the understanding of the mmWave-to-optical conversion process.

1.1. PCB assembly

1.1.1. Radar selection

Current advances in commercial mmWave electronics focus primarily on radar sensors tailored for the automotive industry. Given the objective of demonstrating continuous wave (CW) operation in the conversion process, it is essential that the radar chip supports this mode of operation. Moreover, due to the practical challenges associated with processing mmWave frequencies on PCB boards, the device must integrate both a frequency generator and a transceiver antenna. This ensures that the radar chip can handle the high frequencies and complex signal processing required for effective mmWave application.

After evaluating market offerings and considering all relevant factors, the decision was made to utilize the TRA_120_045 chip developed by Sillicon Radar. This chip features a frequency bandwidth of 20 GHz with maximum output power at around 130 GHz. Its signal generation mechanism involves a voltage-controlled oscillator (VCO) driven by two analog tuning inputs, which feed the output into a low-noise amplifier and a transceiver antenna. The antenna supports a range of up to 5 meters, extendable to 100 meters using dielectric lenses, which is adequate for the typical dimensions of an optical table. For PCB integration, a 64-divider processes and routes the signal to one of the output pins. This setup facilitates the implementation of a frequency locking mechanism employing a phase-locked loop (PLL) and a stable reference oscillator, enabling CW mode emission.

Given the absence of other suitable candidates for the radar chip, the decision was made to proceed with the TRA chip. The experiment was fine-tuned to operate at its most optimal frequency. Using the Alkali Rydberg Calculator [13] Python library, the appropriate state transition was identified, leading to the development of the state diagram illustrated in Fig. 1.

1.1.2. Phase-locked loop

Phase-locked loop (PLL) circuits are indispensable in high-frequency applications, serving as control systems for voltage-controlled oscillators (VCOs) such as the one utilized in the TRA chip. This particular VCO is dependent on two tuning voltages that collectively adjust the resonant circuit, facilitating the generation of a broad range of frequencies. PLLs generate requisite signals for these components by sending a divided feedback signal and a reference frequency f_{REF} into a phase frequency detector (PFD). This circuit compares the two signals, generating an error signal that adjusts the tuning voltage to achieve stable frequency locking. The current sources within the PFD, known as the charge pump (CP), are critical in this process. Given the challenges in accessing sufficiently fast reference signals for high-frequency generation—often the objective itself—additional dividers are employed. In this setup, an N-Integer PLL, specifically the ADF4108 by Analog Devices, was selected due to its availability and suitability for upconversion tasks. This device features, along with the aforementioned components, two programmable dividers, labeled R and N, for the reference and feedback signals, respectively. The N divider includes a prescaler that facilitates the use of standard binary counters, A and B, which are also programmable. This configuration allows the VCO frequency f_{VCO} to be determined and adjusted, using this formula:

$$\frac{f_{VCO}}{64} = \frac{N}{R} f_{REF} = \frac{P \cdot B + A}{R} f_{REF}. \tag{1.1}$$

In the realm of analog electronics, especially within high-frequency synthesis, noise considerations are paramount. Unintended by-products such as phase noise or spurious frequencies (spurs) are critical parameters in evaluating the performance of PLLs. These spurs, often resulting from currents leaking from the charge pump, can alter tuning voltages and consequently the output frequency. A standard mitigation strategy involves incorporating a low-pass filter, which is a common feature in N-Integer PLL configurations, as illustrated in Fig. 1.1. This approach helps minimize the impact of noise on the stability and accuracy of the frequency output.

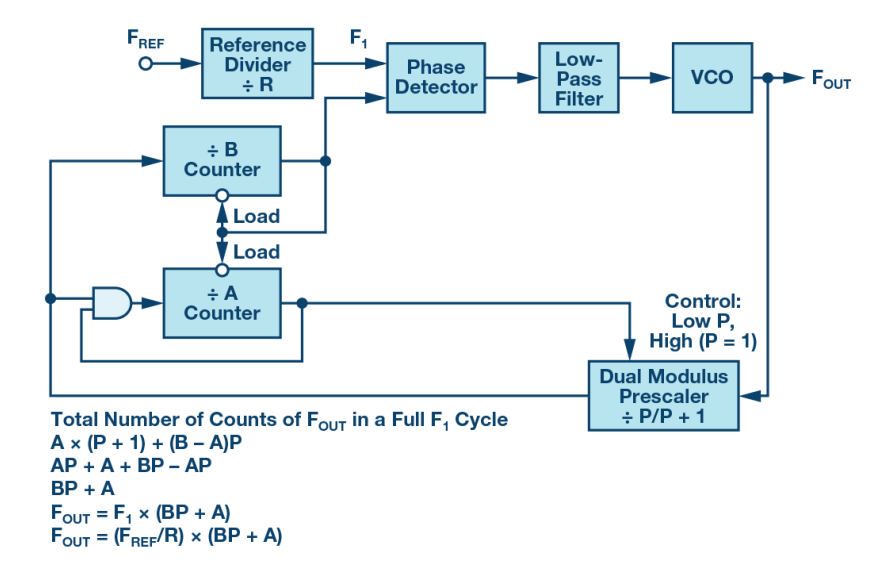


Figure 1.1: N-Integer PLL schematic, as outlined by the producer [14]

In practice, employing a single low-pass filter often fails to achieve the desired stability in high-frequency applications. Consequently, more sophisticated circuits, known as loop filters, are implemented to enhance performance. Additionally, a specifically designed circuit has been integrated onto the PCB to effectively translate the CP signal into the appropriate tuning voltages necessary to drive the VCO.

1.1.3. Frequency locking tests

The assembled PCB, now referred to as the TRA board, incorporates ADF and TRA chips. Control of the TRA board is facilitated by the remotely controlled RedPitaya STEMIlab 125-14 board, a multifunctional device offering typical microcontroller features such as GPIO pins, alongside a full Linux installation and an FPGA chip. The board is managed remotely via Python, and several units are already integral to the existing experimental setup for microwave conversion. The codebase has been expanded to include functionalities for controlling the TRA board, primarily through SPI protocol communication with the ADF chips and by configuring the necessary registers.

Moreover, the ADF chip features an output multiplexer, or MUXOUT pin, which provides access to various internal signals. Connecting an oscilloscope probe and selecting the desired output via the SPI enabled observation of the signals entering the PFD, specifically the reference and feedback frequencies post-division. The lock detect functionality, which leverages an internal phase error threshold, proved particularly useful. Initial testing with a B&K Precision 4087 function generator as reference commenced to evaluate the design of the PLL and its locking capability.

Employing Eq. 1.1, appropriate divider values were selected to achieve an upconversion of a 100 MHz reference to the desired VCO frequency f_{VCO} , given the maximum output of the generator of 120 MHz. Adjusting the reference frequency allows for finer control over the TRA output frequency compared to modifying the divider values, aiming to lock at the desired $f_{mmW} = 130,726$ GHz center frequency with a 100 MHz span for detuning and a

step size of a few MHz. Initial tests with the MUXOUT pin indicated that higher divider values increased noise, prompting the imposition of constraints to maintain these settings as minimal as possible.

Verification of the locking was performed using the lock detection feature of the ADF MUXOUT, which initially showed instability, especially at the target frequency. Adjustments to the charge pump current and the anti-backlash pulse width were made to refine the impact of the error signal on the tuning voltage. Successful stabilization was achieved using the lowest feasible divider values, specifically $N = B \cdot P + A = 3 \cdot 8 + 0 = 24$ and R = 1. Not only was the A register set to 0, but the ratio of N/R was an integer, with both settings contributing to minimizing noise. Before experiments were conducted on Rydberg atoms, it was confirmed that mmWaves were indeed being emitted. Since the TRA chip also functions as a radar with both a transceiver and a receiver antenna, an additional oscilloscope probe was connected to its output pin to monitor changes in the signal when metal objects were moved in front of the chip. Upon successful validation, the board was transferred from the workshop to the experimental setup.

1.2. Autler-Townes splitting

Before analyzing the results, a brief overview of the expected observations is necessary. As light traverses the hot atomic vapor, it is absorbed by the medium. In this experiment, the probe field is finely tuned near resonance to the $5^2S_{1/2} \rightarrow 5^2P_{3/2}$ dipole transition. The resulting absorption spectrum is not a simple narrow line due to the motion of the atoms, causing Doppler broadening, which can be mathematically described by solving the GKSL (Lindbladian) equation for a two-level quantum system interacting with a classical external field [15].

A third energy level, $34^2D_{5/2}$, is introduced to further explore the system. By applying the same analysis used for the two-level system, the GKSL equation is solved to determine the electrical susceptibility of the medium, where its imaginary component dictates the absorption spectrum. A secondary field then couples the excited $5^2P_{3/2}$ state to the $34^2D_{5/2}$ state, effectively linking this highly energetic state with the ground state [15]. This interaction fosters two-photon coherence, manifesting as EIT, where the absorption spectrum of the probe field reveals an additional transparency window corresponding to this new transition. The decay rate of the excited state significantly affects the decoherence rate, making alkali Rydberg atoms ideal for harnessing EIT, due to the long lifetimes of Rydberg states [16, 17]. In strong coupling scenarios, the absorption resonance splits into two — a phenomenon known as A-T splitting or the AC Stark effect, driven by the same principles as EIT but differentiated by the intensity spectrum of the coupling field. The separation of these resonances is directly proportional to the Rabi frequency of the transition between excited states, allowing for direct measurement of the coupling field amplitude. This stems from the change in the probe field linear susceptibility χ_p , which for a 4-level system, with states labeled from 0 to 3 and transitions driven by the probe, coupling and mmWave fields, respectively, is given by:

$$\chi_p = \alpha_0 \frac{\gamma_1}{\gamma_1 - i\delta_1 + \frac{|\Omega_p|^2}{\gamma_2 - i\delta_2} + \frac{|\Omega_c|^2}{\gamma_2 - i\delta_2 + \frac{|\Omega_{mm}|^2}{\gamma_3 - i\delta_3}}}$$
(1.2)

where α_0 is the absorption coefficient in the absence of EIT, $\gamma_{1,2,3}$ are the decay rates of given states, $\delta_{1,2,3}$ are detunings or differences between the applied field and the transition frequency and $\Omega_{p,c,mm}$ are Rabi frequencies of the transitions.

Incorporation of additional atomic levels introduces nested resonances within the absorption spectrum [15]. Each additional field introduces an additional decrease in the effect introduced by its predecessor. Notably, in the 4-level case, the A-T splitting from mmWaves manifests itself not within the absorption resonance but rather within the EIT peak. Eq. 1.2 is a simplified model that does not take into account Doppler broadening, arising from temperature and atom movements. In such a model, the separation is determined by the equation $\Delta_{sep} = \frac{\lambda_c}{\lambda_p} \Omega_{mmWave}$, where the Rabi frequency of the third field (mmWaves) is scaled by the wavelength ratio of the coupling and probe fields. This is visualized in Fig. 1.2. Thus, the A-T splitting of the EIT peak is directly proportional to the amplitude of the incoming mmWave electric field. The strong coupling regime must therefore be avoided, so as the observed splitting, a primary objective in testing the TRA board in subsequent experiments, remains mmWave driven.

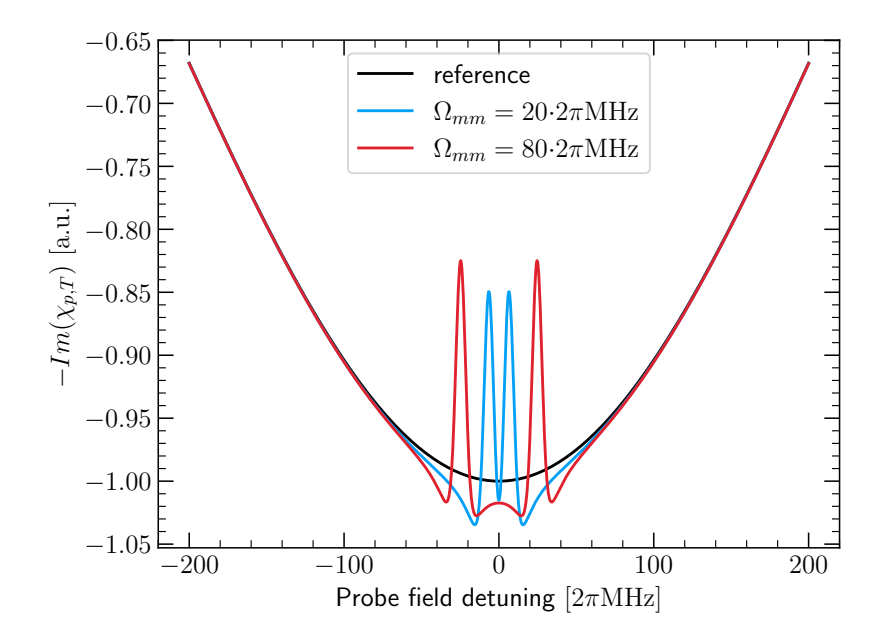


Figure 1.2: The negative absorption coefficient plotted with respect to the probe field detuning. The resulting plot takes into account the Doppler broadening and assumes parameter values taken from experiment. The reference is the regular absorption line, while the blue and red ones showcase the EIT and A-T splitting arising from introducing the coupling and mmWave fields. The higher the mmWave electric field amplitude, the higher the Rabi frequency, resulting in proportionally larger peak separation. The T in $\chi_{p,T}$ stands for temperature, which affects the magnitude of Doppler broadening.

1.3. Existing experimental setup

Although assembling the setup is outside the scope of this work and has been described elsewhere [1, 18], a quick overview will be provided here. The atomic vapor cell is placed at the optical table and excited using several laser sources. Each of them is frequency stabilized using the Pound-Drever-Hall (PDH) technique, with the Koheras Boostik telecom laser serving as the reference. Frequency can be adjusted by frequency shifting the reference, while a 4-f optical setup allows for convenient spatial and angular matching of the laser beam to the atoms. Finally, half- and quarter-waveplates are utilised for attenuation and polarization control.

All of the fields are overlaid onto one another using dichroic mirrors, with the probe field counter-propagating to offset Doppler broadening. The coupling and decoupling fields are filtered out using low- and high-pass filters, so that only the converted signal reaches the detectors. On the other hand, the probe field is sent to a photodiode to measure the transmission spectrum.

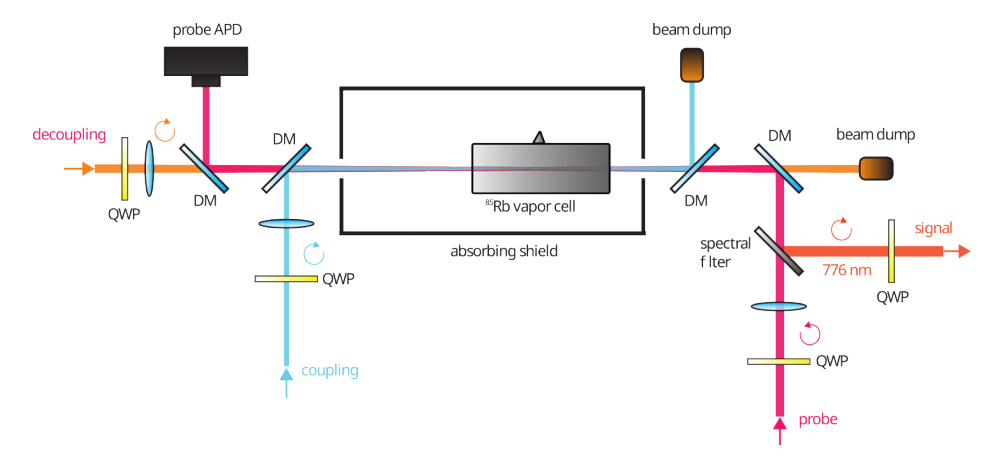


Figure 1.3: The experimental setup before the introduction of the mmWave source. The probe, coupling and decoupling fields are all overlaid and focused on the rubidium vapor cell inside of a microwave absorbing shield. Dichroic mirrors (DM) are used to align the beams colinearly. Quarter-waveplates (QWP) turn the linear polarization into a circular one, which drives a dipole transition with the highest dipole moment. The coupling and decoupling fields go into beam dumps after going through the cell, while the probe goes into an avalanche photodiode (APD) to measure the transmission spectrum. Upon introducing the mmWave field, a resulting optical signal will be produced and has already been marked on the setup.

1.4. Atomic vapor test

To solely observe the A-T splitting, the absorption shield was removed, and the TRA board was positioned adjacent to the Rydberg atom vapor cell. The splitting became immediately apparent during preliminary tests that included free-hand movement. Subsequently, the board was placed on the optical table and meticulous adjustments to its position, height, and angle were made to optimize the visibility of the effect. However, alongside the A-T splitting, additional oscillations in the signal envelope were detected, exhibiting a fixed frequency. Given

that the modulation of the incoming field is directly translated into the modulation of the observed spectrum, it was evident that the system contained unwanted frequency components.

To address this issue, the reference frequency generator was replaced with a more advanced model. The choice fell on the Texas Instruments LMX 2595 synthesizer, a unit from the same family as the microwave source used in the previous experiment [1]. This change led to a noticeable reduction in the oscillations. Notably, in the prior experiment where the LMX signal was directly fed to the antenna, no such oscillations were observed in the frequency spectrum. Since the reference setup was now consistent with earlier configurations, it was concluded that the source of the noise originated from the upconversion process, necessitating further adjustments on the TRA board.

1.5. Eliminating the frequency spurs

To accurately diagnose board issues, it was relocated to the workshop where the feedback signal from the TRA chip was analyzed using an Agilent E4408B spectrum analyzer. The analysis confirmed that while the central frequency appeared as a desired narrow line, there were numerous discrete frequency spurs present. Given that PLLs are fundamentally oscillators, their frequency stability is crucial, especially when evaluated using a spectrum analyzer, which can examine fluctuations in the subsecond variation regime. The observed spectrum displayed a broad skirt accompanied by a series of evenly spaced discrete peaks, known as spurious components, or simply spurs. These spurs may originate from clock frequencies in the signal source, power line interference, or mixer products. The broadening of the spectrum is primarily due to phase noise, potentially caused by thermal instability, shot noise, and flicker noise in both active and passive electronic components [14].

As depicted in Fig. 1.4, the phase noise level is at -60 dB relative to the central peak, while the spurs are tightly spaced at approximately 20 kHz and exhibit an intensity of -20 dB. This level of noise significantly affects the clarity of the transmission spectrum.

Spurs are generally caused by unwanted pulses generated by the PFD that subtly alter tuning voltages. To address this, adjustments were made to the charge pump settings and the circuitry between them and the TRA inputs. Adjustments to the divider values resulted in minor changes in spur separation and a reduction in the intensity of the central peak. Increasing the CP current improved the issue to some extent, but only up to a threshold beyond which the frequency could no longer be locked. Adjustments to anti-backlash pulse width did not yield a significant improvement over the default settings.

The focus then shifted to the loop filter design, the aforementioned circuit between the CP and the VCO. Inspired by the TRA datasheet, the initial design incorporated a third-order passive low-pass filter. The output, operating up to 3.3 V as specified for the ADF, was routed to the VT pin on the TRA chip. In addition, it was channeled through a buffer filter into an inverting operational amplifier to generate a secondary tuning voltage, which was directed to the ICTL pin. During hands-on debugging of the board, it was discovered that one of the tuning voltage inputs exhibited negligible resistance, suggesting damage from the design. The datasheet specifies that two inputs are necessary to maintain the stability of the VCO, so it was concluded that the broken voltage input was degrading the stability of the frequency.

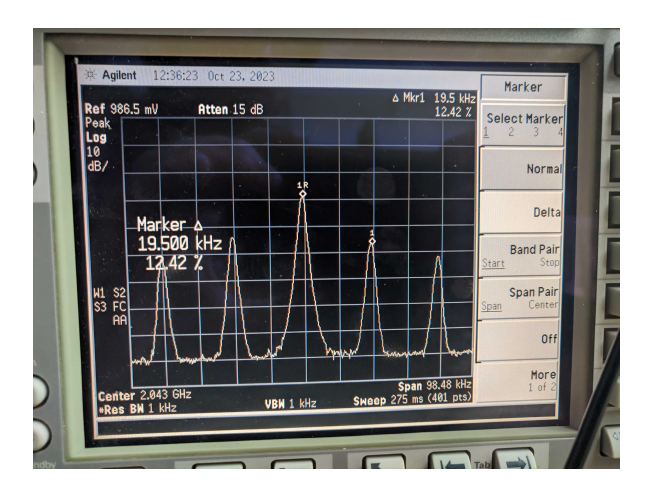


Figure 1.4: Picture of the TRA chip control signal visualized using a spectrum analyzer. The central frequency corresponds to approximately 131 GHz divided by 64. It is clearly dominant with other spurs being almost 20 dB weaker. They are spaced by around 20 kHz, making the spectral lines themselves relatively narrow; however, the lines might be broadened by the device resolution.

Consequently, with the assembly of a new board, it was decided to align the schematic more closely with that recommended in the datasheet. Fig. 1.5 illustrates the differences between the original and the updated schematics. The revised design, which accurately implemented the two driving voltages, did not completely eliminate the spurs but reduced them to an acceptable level of -30 dB relative to the central peak. This reduction was considered satisfactory, particularly since the additional modulation had minimal visibility in the transmission spectrum.

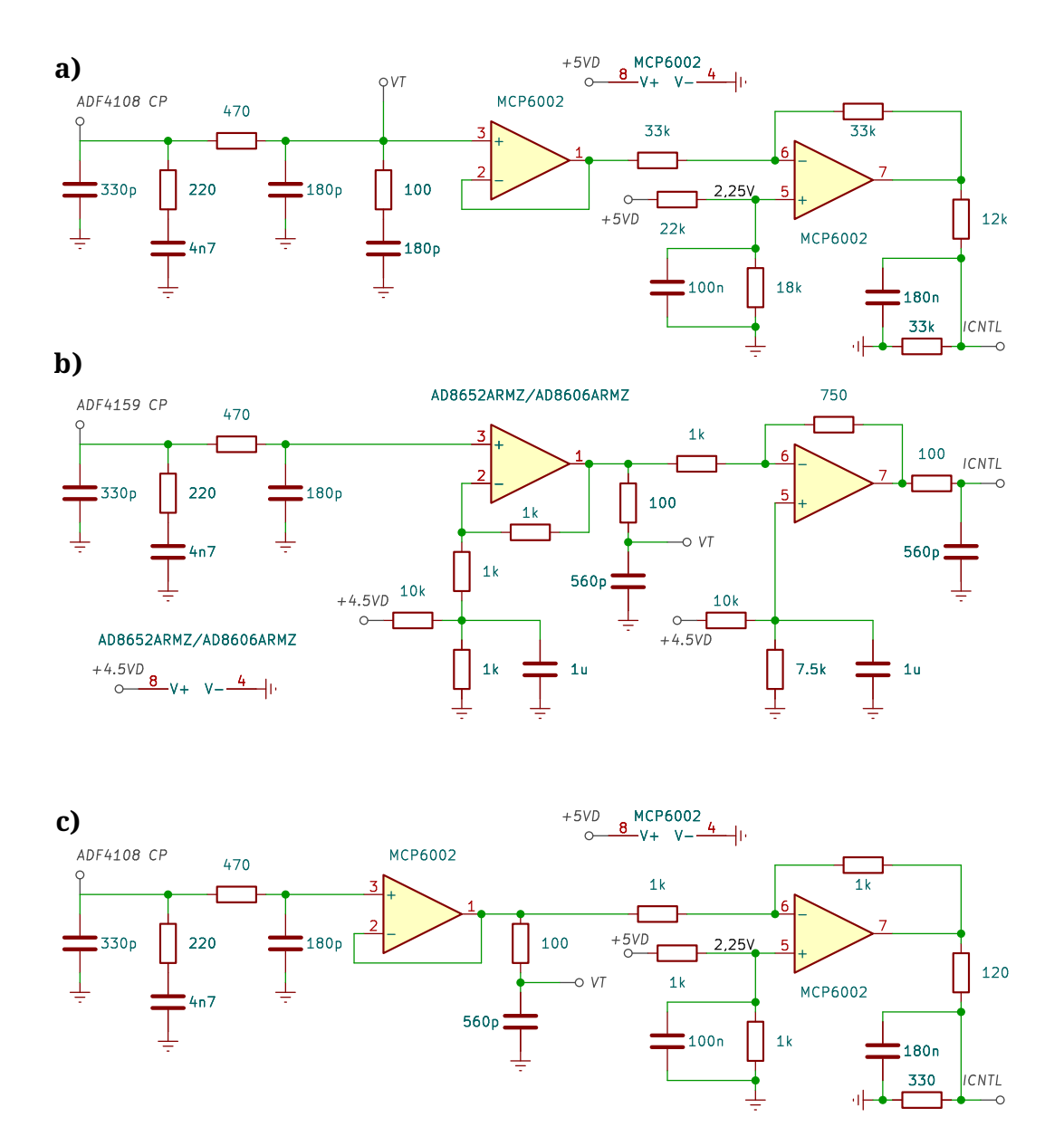


Figure 1.5: Electronic schematics depicting various loop filter designs. Each of them features a charge pump current input, passive filter stage and then operational amplifiers that translate the voltage into the ranges accepted by the VT and ICNTL driving pins. Subfigure a) depicts the first TRA board design that resulted in a fried ICNTL input. When looking at the schematic proposed in the TRA datasheet, as recreated in subfigure b), one can see notable differences in chosen resistance values and most importantly the active noise filtering before the VT input. Adjustments were made on the same PCB, so the changes were limited in scope and resulted in the schematic visible in subfigure c). The VT voltage is now supplied in the same way as in the datasheet, and the resistances were dropped to similiar values. While the power supply differences look considerable, they actually have little to no effect on the PLL.

Chapter 2

Initial measurements

2.1. Conversion measurements

Observing the A-T splitting was initially facilitated by simply positioning the board adjacent to the rubidium cell. However, the conversion parametric process crucially depends on the phase matching of all electric fields. Therefore, the initial setup involved aligning the board to be collinear with the laser beams. Initially, the board was positioned just above the mirrors that channeled the beams into the cell, while the radiation shielding remained removed. Although the alignment was not perfectly collinear, it was considered adequate given that the radar chip emitted mmWaves at a broad angle. A Basler acA2500-14gm camera was installed at the output of the setup, positioned after a series of filters that eliminated driving fields, to monitor the generation of an optical signal.

2.1.1. Conversion setup process

The laser beams had already been correctly directed into the rubidium cell, thus the initial task involved fine-tuning their frequencies to align with new state transitions. While the probe laser settings remained unchanged, both the coupling and decoupling fields required adjustments. The adjustment of the first was achieved by examining the EIT in the transmission spectrum and positioning its peak at the desired detuning, consistent with the previous experiment [1]. Following the adjustment, frequency locking was activated, and A-T splitting was observed again by reactivating the TRA board. Adjustments were made to the position and frequency to maximize the effect. Effectively, the goal was to optimize the left hand side of the transition loop depicted in Fig. 1. The same process was replicated for the right hand side to optimize the decoupling laser, with an auxiliary laser beam, tuned to the output frequency. After all electric fields were adjusted to the appropriate dipole transitions and their frequencies stabilized, the probe laser was locked.

The auxiliary laser was then deactivated, and the Basler camera was set to long exposure to detect any emerging optical signals, which were faint but noticeable, indicative of a weak conversion process. Further adjustments were made to the beam positions, polarizations, intensities, and frequencies, each aimed at maximizing the detected signal. Even with sub-

optimal phase matching, the converted output beam was clearly visible through the camera. The intensity matched that observed in the prior experiment, affirming the suitability of the TRA chip as a signal source.

The positioning of the TRA board was provisional, and an alternative setup was soon tested. Previously, a radiation shield filtered out potential environment radiation, allowing only minimal laser entry and exit, as well as prevented unwanted reflections. With the prior antenna setup internalized, a new method was devised to direct mmWaves collinearly with the lasers, utilizing a dielectric lens to collimate the TRA output. Initially positioned at a distance from the cell, the arrangement facilitated notably intense A-T splitting. The beam waist remained consistent, confirmed by a shutter placed at various points along the beam path. Once optimal positioning was established, the assembly was relocated behind the dielectric mirrors channeling the laser beams into the rubidium cell. The attenuation of the mirrors proved small enough to maintain visible A-T splitting. Additional fine-tuning of the TRA and lens positions was guided by feedback from the conversion camera, enhancing the intensity of the results.

Precise measurements necessitated the use of a photon counter instead of the camera. To fiber couple the converted signal, two cameras were employed in both near- and far-field positions. The auxiliary 776 nm laser was adjusted to propagate collinearly with the conversion signal, visible to both the naked eye and the power meter. Fiber coupling was performed on this laser field, with the photon counter initially disconnected. Once aligned, the laser was deactivated, and the fiber was linked to the ID Quantique ID281 superconducting nanowire single-photon detector, which successfully captured the conversion signal. Subsequent optimizations were guided by the photon counter readout, involving fiber coupling and other previously adjusted beam parameters. The use of neutral density (ND) filters was required as photon counts reached 10⁷ photons per second, a level where detector dead times significantly impact measurement accuracy causing unwanted saturation of detectors.

2.1.2. Bandwidth and autocorrelation

Measuring the bandwidth is a straightforward task, involving only the recording of photon counts across various TRA frequencies, which can be adjusted by altering the LMX reference frequency. The resulting data are presented in Fig. 2.1, where the conversion band, defined as the full width at half maximum (FWHM), equals 22 MHz.

Subsequently, autocorrelation measurements of thermal radiation were undertaken. A 50:50 fiber beam splitter was installed prior to the single-photon counter and connected to separate detector inputs. With the TRA chip deactivated, all detected photons were solely due to thermal mmWave photons interacting with the rubidium cell. An extensive overnight measurement yielded the second-order autocorrelation function $g_2(\tau)$, depicted in Fig. 2.2. The data were then compared with the theoretical model from the previous microwave-based experiment. Employing the Wiener-Khinchin theorem:

$$g_{th}^{(1)}(\tau) = \frac{1}{2\pi} \int_{-\infty}^{\infty} |S(\omega)|^2 e^{-i\omega\tau} d\omega = \mathcal{F}^{-1}\{|S(\omega)|^2\},\tag{2.1}$$

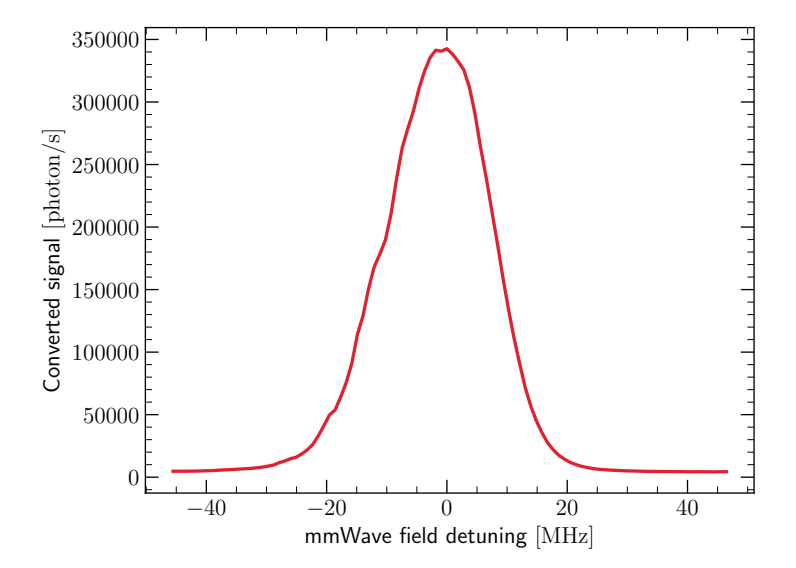


Figure 2.1: Measured photon counts for a range of mmWave frequencies around the resonance. The TRA output frequency was controlled by tuning the reference RF signal. The output mmWave frequency was then calculated using known divider values. The values on the x-axis are the mmWave field detunings from the resonant value obtained using the ARC library.

allows for the calculation of the first-order autocorrelation function of thermal radiation $g_{th}^{(1)}$ from the normalized power spectral density $|S(\omega)|^2$, initially measured to determine the bandwidth (shown in Fig. 2.1). Assuming that thermal radiation behaves as white noise, independent of frequency, the second-order autocorrelation function is then given by:

$$g_{th}^{(2)}(\tau) = 1 + |g_{th}^{(1)}(\tau)|^2.$$
 (2.2)

This relationship, combined with Eq. 2.1, enables the plotting of the function shown in Fig. 2.2. It was evident that the experimental data did not align well with the theoretical predictions, prompting a reevaluation of the theoretical model to consider additional phenomena potentially influencing the discrepancies.

2.2. Conversion of thermal radiation

2.2.1. Derivation

While the reevaluation of the theoretical model is beyond the scope of this work, another measurement was concurrently performed to estimate the effective electric field root-mean-square (RMS) amplitude of thermal blackbody radiation, following the derivation used in the prior microwave experiment [1]. The effective RMS electric field $\sqrt{\langle E_{eff}^2 \rangle}$ is determined by:

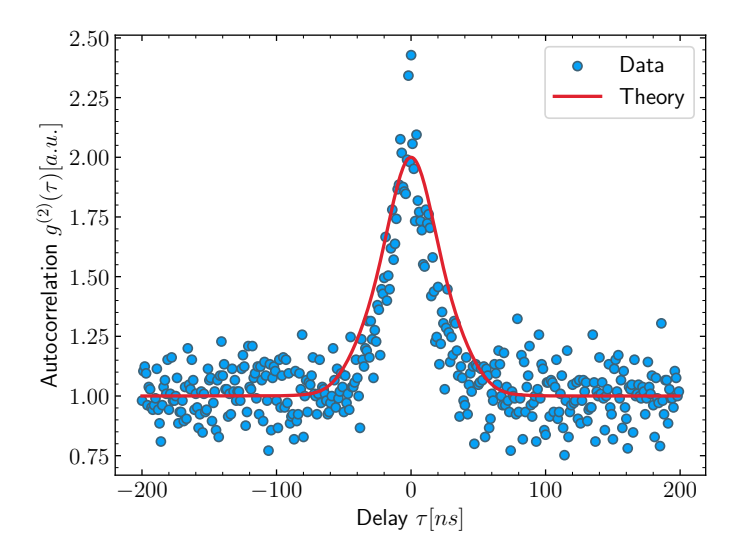


Figure 2.2: Measured autocorrelation of thermal photons. The time delays were calculated by the time controller using predefined time bins and the measurement was performed overnight with the TRA board turned off. The theoretical line was obtained using the measured bandwidth from 2.1 and the Wiener-Khinchin theorem.

$$\langle E_{eff}^2 \rangle = \frac{\omega^2 \langle \mathcal{E} \rangle}{\pi^2 c^3 \varepsilon_0} \frac{1}{4\pi} \int_0^{2\pi} d\phi \int_0^{\pi} d\theta \sin(\theta) |\eta(\theta)|^2$$
 (2.3)

$$\langle \mathcal{E} \rangle = \frac{\hbar \omega}{e^{\frac{\hbar \omega}{k_B T}} - 1} \tag{2.4}$$

Here, ω is the frequency of the mmWave field, c is the speed of light, ε_0 is the vacuum permittivity, k_B is Boltzmann's constant, T is the temperature, and $\eta(\theta)$ represents the efficiency of the conversion process, which accounts for phase matching and the projection of mmWave field modes onto the circular polarization along the conversion axis at angle θ . $\eta(\theta)$ has been numerically calculated, facilitating the estimation of the expected RMS amplitude due to thermal black body radiation.

2.2.2. Measurements

The conversion of thermal photons was monitored using the single photon counter. After optimizing the mmWave conversion setup, the TRA board was powered down to ensure that only thermal radiation and dark counts were measured. Covering one of the conversion-enabling lasers resulted in a tenfold reduction in photon counts, confirming ongoing conversion from background thermal radiation. However, these photon counts alone do not provide sufficient information to deduce the electric field amplitude. This is extracted from the A-T splitting observed in the probe transmission spectrum. The distance between peaks of the split EIT resonance, when mmWave field detuning is negligible, equals the Rabi frequency

 Ω_{mm} of the mmWaves, scaled by the Doppler wavelength proportion $\frac{\lambda_c}{\lambda_b}$. The Rabi frequency is defined as proportional to the electric field amplitude by:

$$\Omega = \frac{dE}{\hbar} \tag{2.5}$$

where d is the dipole moment associated with the state transition, determined using the Alkali Rydberg Calculator (ARC) library [13]. Estimating A-T splitting is straightforward for significant separations, but becomes challenging with smaller separations akin to resolving two closely spaced Gaussian pulses, where precision rapidly diminishes. Therefore, accurate electric field estimations are feasible only when the field strength is sufficiently large. To address low field strength measurements, it was necessary to parameterize the relationship between the electric field and photon counts in a measurable range and extrapolate this relationship to the thermal limit. Unfortunately, the TRA board lacks a continuously adjustable transceiver amplifier, limiting adjustments to off, on, or high power modes, with only the unamplified signal being weak enough to avoid saturating the photon counter. Consequently, a method of attenuation with a linear response in free air needed to be devised and tested, ensuring it provided continuous variability.

2.2.3. Attenuator

Picking the right material

Given that mmWaves more closely resemble the THz regime than the microwave band, options for existing solutions are limited. Rather than relying on emerging commercial products, initial experiments were conducted with materials readily available in the laboratory. The preliminary approach involved positioning various media between the TRA transceiver and the atomic vapor cell. Since mmWave attenuation was readily observable by simply obstructing the beam with a hand, it was promising to explore materials with significant absorption properties and adjust their thickness accordingly.

Several materials were tested, starting with sponge-based absorbers typically accompanying RF equipment, and a specialized carbon foam designed for microwave shielding. The sponge absorbers provided minimal attenuation, less than 1 dB, indicating that a substantial volume would be necessary for effective attenuation. Conversely, the carbon foam exhibited impressive attenuation levels of over 10 dB. However, its structural properties posed challenges: it crumbles easily and achieving a smooth surface is problematic. Additionally, its high absorption rate meant that even minor variations in thickness could introduce significant errors in the measurements.

Given the small wavelength of mmWaves, which allows them to propagate following geometric optics principles while still exhibiting diffraction effects on millimeter-scale structures, further tests were conducted. Prototype PCB boards and wired plate heaters were evaluated for their attenuation properties, both offering significant attenuation with well-defined and minimal thicknesses. The latter proved particularly intriguing due to its angle-dependent attenuation, suggesting that its embedded metallic wires, spaced approximately 0.3 mm apart, function as a linear polarizer for the mmWave signal. This discovery indicated that the limita-

tion of discrete attenuation steps typically associated with universal plates could be mitigated. By arranging multiple polarizers in the form of plate heaters and mounting one on a rotor, a more controlled and adjustable attenuation setup was achieved.

Polarizer based attenuator

The concept implemented involves a series of four polarizers. Initially, these were aligned sequentially along the path of mmWaves, which traveled from the TRA board through dielectric mirrors and into the atomic vapor cell. The polarizers were oriented identically to evaluate if the attenuation contribution from each was consistent. However, findings indicated that photon count changes were highly sensitive to the distances and angles between each polarizer, suggesting multiple reflections and necessitating a different configuration.

Reflective losses from the metallic wires in the polarizers were significant, prompting an arrangement where the mmWave signal would reflect at right angles off all plates, ensuring that no transmitted part would interact with other components. Due to spatial constraints around the atomic vapor cell, both the TRA board and the polarizers were relocated to the side of the setup. A metallic plate with a central hole was positioned adjacent to the setup, so as to reflect the incoming mmWaves at a right angle, while allowing the lasers to propagate through the hole.

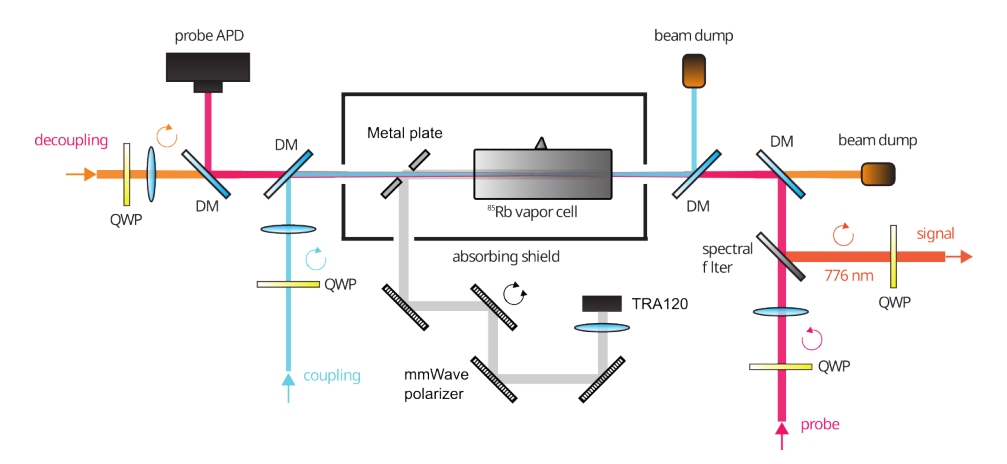


Figure 2.3: The experimental setup with the TRA board and the polarizer based attenuator. The radar signal is collimated and sent through 4 polarizers, one of which is placed on a rotating setup. The mmWave field is reflected, not transmitted through the polarizers to avoid multiple reflections. A hole was made on the side of the absorbing shield to let the beam in from the side. Its much larger waist makes reflecting it from a metal plate with a small hole possible. The rest of the setup from Fig. 1.3 remains unchanged.

At this stage, four polarizers were employed. The orientations of the first and last polarizers were fixed, optimized in subsequent adjustments to maximize intensity towards the source and target, respectively. The second plate was also fixed to enhance the polarity of the beam, as these plates were not ideal polarizers. These non-rotating polarizers were mounted on 3D-printed handles, allowing for vertical or horizontal polarization when oriented appropriately. The optimal polarizations were determined by rotating the third polarizer by 45 degrees and adjusting the remaining polarizers accordingly. As detailed in Table 2.1, the source exhibited

a stronger horizontal polarization, while vertical polarization more effectively aligned with the circular polarizations necessary for driving the conversion process.

Name	Pol. 1	Pol. 2	Pol. 3	Pol. 4	${f Photons/s}$
НН	\iff	\iff		\iff	13.3M
VH	1	1		\iff	7.5M
HV	\iff	\iff		1	17.8M

Table 2.1: Converted photon counts for different polarizer configurations. Arrows indicate the orientation of each polarizer, while the last column specifies the measured photon counts, with 1M corresponding to one million photons.

Calibration

With a functional attenuator now in place, it became feasible to measure the relationship between photon counts and the incident electric field at various intensities. After recording several A-T splittings and their corresponding photon counts, the TRA was deactivated, and the counts from converted thermal photons were recorded. Subsequently, dark counts were also documented with the decoupling laser deactivated. To ensure accuracy in the upcoming calculations, the bandwidth measurement was repeated, updating the previous data collected several days earlier.

The procedure allowed for the determination of thermal converted photon counts, adjusted by subtracting the dark counts, which corresponded to an equivalent coherent field of 14.18 · $10^{-3} \ V/m$. Assuming the thermal field was constant across the measured bandwidth, the integral conversion bandwidth was calculated. The measured bandwidth was normalized to unity and then integrated numerically. The equivalent coherent field was divided by the fraction of this normalized value to estimate the spectral density of the thermal field itself, which was found to be $1.16 \cdot 10^{-6} \ V/m \ (rad/s)^{-\frac{1}{2}}$ or $11.6 \ nV/cm \ (rad/s)^{-\frac{1}{2}}$.

The estimated value was then compared to the theoretical effective root mean square amplitude of the field, calculated to be 15.3 $nV/cm \left(rad/s\right)^{-\frac{1}{2}}$. The ratio of their squares, representing the thermal mode coupling coefficient, was calculated to be 0.58. The divergence from the ratio of 1, meant that there are significantly less thermal photons being converted, in comparison to coherent ones, emitted by the TRA board.

The observed theoretical discrepancy prompted further questions and doubts about the current theoretical model. Together with the autocorrelation measurement, it was indicated that there are simply too many photons being emitted by the TRA board, i.e. the actual bandwidth could be much smaller. In response, additional tests were performed using an adjusted optical bias microwave detection setup [19]. This modification involved omitting the reference microwave local oscillator (LO), which limited spectral precision to the collective noise of the optical fields. Despite these constraints, it was possible to observe that the spectral width of the emitted mmWave radiation was approximately 800 kHz. This suggested that the chip design might be flawed, with the locking mechanism proving insufficient to stabilize the TRA radar frequency effectively.

In light of these findings, efforts were initiated to redesign the electronic setup. However, pending these improvements, it was decided to explore an optical approach to mmWave generation using a photomixer, which is commonly employed for generating continuous wave terahertz frequencies. This alternative method was anticipated to offer a more stable generation platform while the electronic adjustments were being perfected.

Chapter 3

Verification using a photomixer

The THz regime presents significant challenges for exploration as a result of the scarcity of adequate equipment, unlike the well-explored RF and optical bands. The TRA approach aimed to access mmWave frequencies through electronics and the process of upconversion. However, an alternative approach involves synthesizing these frequencies from the higher energy optical band. THz frequency synthesis via optical methods is rapidly evolving, employing various technologies including photoconductive switches, optical rectification, and quantum cascade lasers. However, these methods predominantly generate THz pulses, rather than the continuous waves necessary for the wave mixing process central to this experiment. Currently, the only method developed that supports continuous wave generation is photomixing, which relies on subtracting two optical frequencies.

3.1. Principle of operation

Similarly to traditional electronic mixers, the objective in THz generation is to subtract frequencies from two higher-frequency fields to produce a lower frequency output. This process involves spatially overlapping two lasers with identical polarization, directed onto a photoconductive antenna (PCA). Interaction of the lasers with the semiconductor material of the PCA induces polarization through a second-order nonlinear process. The requirement for short carrier lifetimes allows the medium polarization to oscillate at THz frequencies, matching the beat frequency of the external fields. This oscillation, in turn, leads to variations in the conductivity of the medium. When a voltage is applied through the metal electrodes and an antenna layer, THz radiation is emitted.

The primary advantage of this setup is its significant frequency tunability, which is achieved by adjusting the frequency of just one of the lasers. Moreover, the spectral stability is predominantly determined by the stability of the optical fields. However, a major drawback is the low power output, inherent to the use of a nonlinear process and exacerbated by the system operating in CW mode.

3.2. Initial test

To verify the operating principle, a BATOP optoelectronics PCA suitable for 800 nm light was procured, and two existing lasers at the lab were employed. The first was a narrowband 1560 nm fiber laser by NKT Photonics, stabilized to a rubidium cell via a modulation-transfer lock. This laser acts as a reference for stabilizing the other lasers in the lab using optical cavities that will be explored in greater detail later. The probe laser is the exception, as it is stabilized using an optical phase-locked loop, where a frequency-doubled reference beam of 780 nm is used. The second laser used for the photomxier was a tunable diode laser from Toptica, also operating at around 780 nm.

Both lasers were directed into a Thorlabs fiber coupler, with the combined output connected to a custom-made fiber PCA connector. All connecting fibers were of the polarization maintaining (PM) type, ensuring identical polarization for the overlapped optical signals. This initial setup, aimed merely at verifying the working principle, utilized the mmWave conversion setup optimized previously with the TRA chip. With the photon counter sensitive enough to detect even weak TRA reflections and background thermal photons, the TRA chip was subsequently replaced by the PCA.

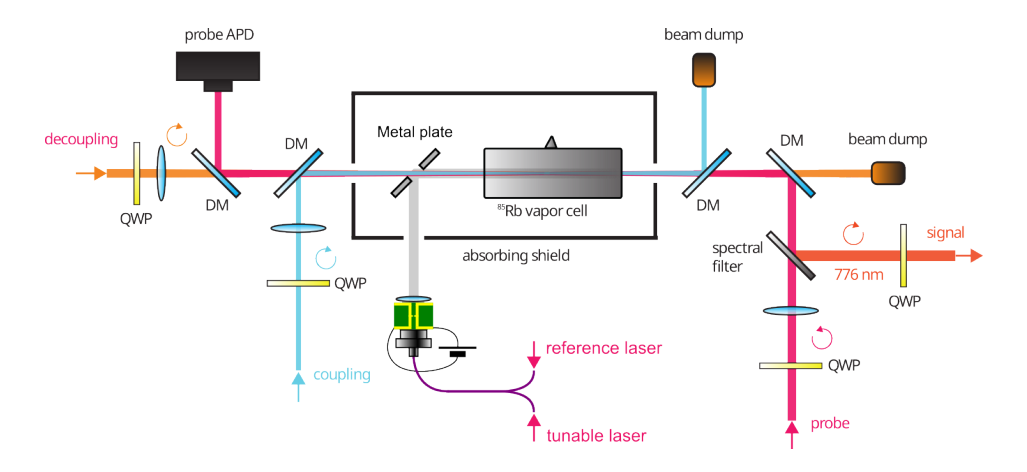


Figure 3.1: The experimental setup with the photomixer used as the mmWave source, instead of the TRA in Fig. 2.3. Two lasers are mixed using a fiber coupler, producing a beat frequency that excites a photoconductive antenna. Together with the applied DC voltage, the antenna produces a mmWave signal that is also collimated using a dielectric lens.

A precise wavelength meter measured the reference frequency, facilitating the calculation and adjustment of the required tunable laser frequency. Continuous monitoring was achieved using the same wavelength meter in conjunction with a beam splitter. Upon reaching the target frequency, a change in photon counts was observed; however, these changes were an order of magnitude smaller than those with the TRA board and were transient, necessitating further adjustments to the laser frequency within seconds. This observation confirmed the functionality of the photomixing process, underscoring the need to develop a frequency stabilization setup for the second laser.

3.3. Pound-Drever-Hall technique

Frequency stabilization is crucial across various physics disciplines, with the PDH technique widely adopted due to its simplicity and effectiveness. This method is pivotal in high-precision experiments in spectroscopy and interferometry, and most notably in the LIGO experiment. Off-the-shelf lasers, though nominally monochromatic, are subject to multiple instability sources, both internal and external, as illustrated in Fig. 3.2. These instabilities are typically offset by comparing the unstable laser with a stable reference and employing a PID (Proportional, Integral, Derivative) controller, which adjusts the tunable laser to prevent long-term drifts and minimize jitters.

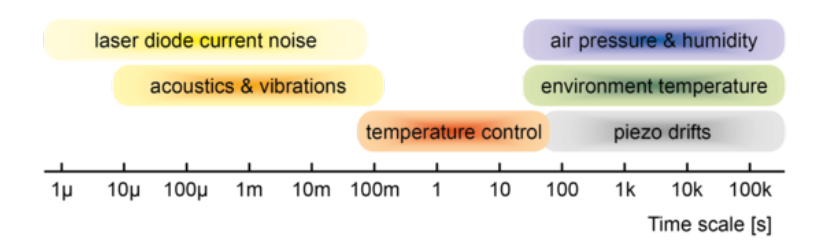


Figure 3.2: Sources of laser frequency instability and time scales in seconds at which they affect the system, from jitters on the left hand side to slow drifts at the right hand side [20]

Numerous sources detail the PDH technique, each varying in depth and focus [21, 22, 23]. This section offers a brief conceptual overview. The underlying principle of the PDH method aligns with other frequency stabilization techniques, with the aim of generating an error signal. This signal is then integrated into a feedback loop within an electronic control circuit. A PID controller processes this error signal to implement corrective actions on the source device, in this case, adjusting the diode current that drives laser emission. The PID acronym represents Proportional, Integral, and Derivative components, each contributing to the system's response dynamics:

- **Proportional:** This component responds to the current frequency deviation from the target value by applying a proportional adjustment. As the error reduces, so does the proportional contribution, which can slow the approach to the setpoint.
- Integral: It accumulates residual errors over time, allowing the system to adjust and stabilize closer to the setpoint, particularly effective in the near-setpoint regime.
- **Derivative:** Often regarded as anticipatory control, this element tempers rapid changes by adjusting corrections based on the rate of change, enhancing system responsiveness and stability.

Generating a proper error signal is fundamental to the PDH technique. This process involves comparing the laser output frequency to a stable reference, typically a Fabry-Perot cavity. Ideally, such a cavity reflects all modes not aligned with an integer multiple of its free spectral range $\nu_{FSR} = \frac{c}{2L}$, where c is the speed of light and L is the cavity length. This

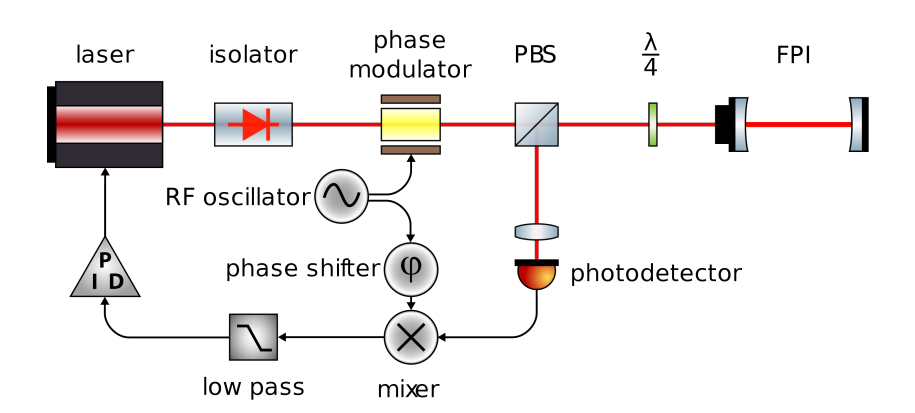


Figure 3.3: Schematic of PDH servo loop to lock the frequency of a laser (top left) to a Fabry–Perot cavity (top right). Light from the laser is sent through a phase-modulator and is then directed upon the cavity. (For diode lasers, fast frequency or phase modulation can be performed by just modulating the diode current, obviating the need for an external electro-optic or acousto-optic phase modulator). The isolator is not involved in the PDH setup; it is present only to ensure that light from various optical components does not reflect back into the laser. The polarizing beamsplitter (PBS) and $\lambda/4$ plate act in combination to discriminate between the two directions of light travel: light traveling in the direction from left to right passes directly through and on to the cavity, while light traveling in the direction right to left (i.e. from the cavity) is diverted toward the photodetector. The phase modulator is driven with a sinusoidal signal from the oscillator; this impresses sidebands onto the laser light. As described in the section on the PDH readout function, the photodetector signal is demodulated (that is, passed through the mixer and the low-pass filter) to produce an error signal that is fed back into the laser's frequency control port. [24]

configuration effectively acts as a filter, with transmission resonances spaced in the frequency domain by ν_{FSR} .

The primary objective is to extract the reflection coefficient dependent on the deviation $\delta\omega=\frac{\omega}{\nu_{FSR}}$ from the intensity of the reflected beam. The reflected beam comprises a coherent sum of the beam immediately reflected off the first mirror and a leakage beam from the standing wave within the cavity. Under resonant conditions, these components are π radians out of phase, leading to mutual cancellation and a zero error signal. Deviations from resonance cause the reflection coefficient to change rapidly, depending on the finesse of the cavity. In particular, this coefficient is a complex number, and its phase varies to indicate whether the frequency is above or below ν_{FSR} , which guides the direction for the laser adjustment.

This reflection coefficient is obtained by modulating the phase of the incident beam using a single RF oscillator and an electro-optic modulator (EOM). Sinusoidal phase variations at frequency Ω introduce sidebands at $\pm \Omega$ relative to the carrier frequency. These changes propagate into the reflected intensity, producing additional terms that vary as $\cos(\Omega t)$ and $\sin(\Omega t)$. These can be demodulated using the same RF frequency and a frequency mixer. The setup is depicted in Fig. 3.3, and detailed calculations are available in the referenced literature [21, 22, 23].

Typically, an optical cavity of known length serves as the reference. To facilitate tuning, a piezo element may be attached to one of the mirrors to adjust the cavity length L as required.

In many cases, including the scenario described here, it proves simpler to use another optical source as a reference, implementing what is known as transfer locking. In this dual application of the PDH technique, the cavity length is first locked to the frequency of the reference field by controlling the piezo based on the reflected intensity of the reference beam. Subsequently, the target laser is locked to the adjusted cavity length. By introducing additional modulation that shifts the reference beam frequency, stable tuning is achieved by programmatically adjusting this shifting RF frequency.

3.4. Assembly of a frequency stabilizer

3.4.1. Cavity setup

The core component of the frequency stabilizer is the Fabry-Perot cavity, designed not only for adjustable length but also for high resistance to external disturbances. The cavity consists of a small metallic tube crafted in the workshop, featuring metal caps with windows and rubber o-rings at both ends. A spherical mirror is positioned beneath one cap, while the opposite end houses a piezo element and a planar mirror. The assembly is secured on a metallic bed using rubber o-rings for vibration damping and encased within a larger tee structure. Two outlets are used by lasers, while the third one is used for connecting the vacuum pump and the piezo amplifier. This setup is later enclosed using windows and a special cap for piezo power cables.

This configuration constitutes a half-symmetric resonator, effectively half of a symmetric resonator but with double the length. Such systems are adept at confining Gaussian beams as standing waves, provided the beam parameters are matched to the geometry of the cavity. The necessary conditions for this alignment are detailed in standard optics texts [25]. Particularly, the resonant Rayleigh range z_R is defined as:

$$z_R^2 = \frac{g_1 g_2 (1 - g_1 g_2)}{(g_1 + g_2 - 2g_1 g_2)^2} L^2, \tag{3.1}$$

where $g_{1,2}=1-\frac{L}{R_{1,2}}$ represent the resonator g parameters, L is the cavity length, and $R_{1,2}$ are the curvatures of the mirrors. In the half-symmetric resonator setup, with $R_1 \to R$ and $R_2 \to \infty$, the equation simplifies to:

$$z_R^2 = \frac{g(1-g)}{(1-g)^2}L^2 = \frac{g}{1-g}L^2.$$
 (3.2)

With the Rayleigh range calculated, appropriate focusing optics can be selected to achieve optimal mode matching with the cavity. This adjustment is necessary for both the 1560 nm reference and the 780 nm tunable laser, noting that each laser enters the cavity from a different side. Constraints included the availability of lenses in the laboratory and the need to maintain space around the vacuum tee for assembly purposes. Gaussian beam propagation and lens placement were modeled using the GaussianBeam software [26], facilitating the selection of suitable lenses and distances.

3.4.2. Optical setup

The entire setup has been assembled on a relatively small optical plate to facilitate future mobility. In addition, the plate was placed on thick sponges to enhance mechanical stability and isolate it from vibrations and disturbances on the shared optical table.

Fiber optics

Both lasers had to be brought in to the setup using fibers. As such, fiber-based EOMs were used to modulate the signal, with couplers positioned at two corners of the optical plate. Collimating lenses were selected on the basis of GaussianBeam software calculations and fine-tuned by projecting the laser light across the lab over several meters. Adjustments were then made to the lens spacing to maintain a consistent beam waist.

The EOM models for the 1560 nm and 780 nm light were iXblue MPZ-LN-10 and NIR-MPX9560-LN-10, respectively. It is crucial for the input light to maintain an appropriate polarization for effective modulation, hence PM fibers were used. At the output, a power meter was employed and polarization was rotated before the fiber input couplers to maximize output intensity to make sure that the EOM-preferred polarization was being used.

Beam propagation

The optical setup, shown in Fig. 3.4, is fundamentally similar for both lasers, differing only in the specific components adapted for their respective wavelengths. After exiting the fiber, the collimated light passes through a half-wave plate (HWP), a polarizing beam splitter (PBS), and a quarter-wave plate (QWP). The HWP adjusts the polarization to maximize transmission through the PBS, while the QWP configures the returning beam to ensure that it reflects off the PBS, preventing it from returning to the coupler. Reflected light from the cavity is directed to a photodiode (PD) sensor using a mirror and a lens to capture the error signal. A mirror placed between the QWP and the cavity, along with the coupler, provides two geometric degrees of freedom for precise spatial alignment with the cavity. Finally, the focusing lens, determined through simulations, is positioned at the calculated distance.

Cavity coupling

Since the process is identical for both lasers, it is possible to first couple one laser and then simply align the other one to be colinear. As this is easier with the 780 nm wavelength, it was decided to begin with it. Initially, the cavity was not placed on the optical plate and both lasers were aligned to be colinear. Then, the vacuum tee with the cavity was placed along with a camera on the 1560 nm side. Before mounting the tee to the plate, rough movements were made by hand, until eigenmodes of the cavity could be observed. Due to the cylindrical symmetry of the resonator, it was expected that it would be one of the Laguerre-Gaussian modes. To mitigate the need to match the multiple of ν_{FSR} , frequency scanning was enabled on the Toptica DLC Pro digital control platform. Indeed, higher order L-G modes were observed and the tee has been attached to the optical plate.

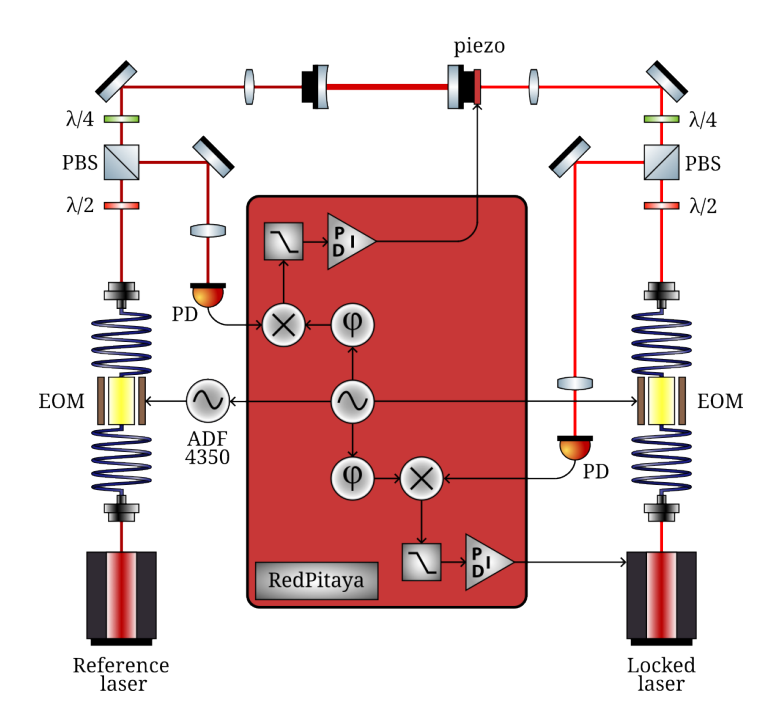


Figure 3.4: Schematic showcasing the frequency stabilizer setup. The reference and tunable laser beam propagate in analogous way and reach the same Fabry-Perot cavity with one planar mirror mounted on a piezoelectric element. Both lasers are modulated using fiber-based electro-optical modulator (EOM), with a frequency of 25 MHz, generated on the RedPitaya board. The reference is additionally frequency shifted by 2,2-4,4 GHz using an ADF4350 frequency generator. Upon leaving the fiber, both lasers propagate through an half-wave plate and a polarizing beam splitter (PBS). In order for the cavity reflected beam to be reflected from the PBS, a quarter-wave plate is placed after it. Focusing lenses are used to match the beam with the base cavity mode and to maximize the signal registered by the photodiodes (PD). The PD signal of the cavity-reflected beam is then mixed with the original LO frequency of 25 MHz, which is also phase shifted to retrieve a proper error signal. The error signals are then low-pass filtered and sent to PID controllers that control the piezo and the tunable laser, effectively locking both the cavity length and the tunable laser frequency to the reference laser.

Subsequently, the spatial matching was improved using fine movements of the mirror and fiber coupler holders, with the goal of obtaining the 00th or simply Gaussian mode, resembling a single circle on the camera. Even more fine-grained corrections can now be made using the PD. Its signal was connected to the DLC Pro input signal and the scanned frequency spectrum could be observed with a constant intensity and discrete resonance dips. Now, the spatial coupling was improved in such a manner, to maximally deepen the resonances corresponding to the 00 mode, while canceling out all the others.

Once that was done, the camera was removed. It was now time to mount the vacuum windows and connect the vacuum pump, since the cavity inside of the tee should not be moved anymore. Once all the tubes, o-rings and clamps were in place, the cavity coupling was once again refined as minor displacements were unavoidable.

Finally, the time has come to couple the second laser. For this purpose the input power of the 780 nm laser has been maximized and the scan was set to be small and close to the

resonance. After turning off all the external lights, it was possible to see a faint transmitted light, to which the 1560 has been aligned. Then, the reflected reference beam was also sent to a PD and resonances could already be observed, so the same procedure as before has been repeated.

3.4.3. Electronic setup

Upon completing the optical part, the time has come to attach all the necessary electronics. The heart of the setup is once again the RedPitaya STEMlab 125-14 board, which features, among others, an FPGA chip, RF analog connectors, and numerous digital I/O pins. Using the lab created software, it can serve as a remotely controlled oscilloscope, I/Q demodulator, PID controller and signal generator, all combined in a single board. This versatility makes it a perfect candidate for managing the electronic part of the setup. As can be seen in Fig. 3.4, the internal clock of the RedPitaya serves as the f_{LO} frequency generator, providing a sine signal of 25 MHz.

This is fed to both EOMs, however, the one modulating the reference beam has an extra step, where it can be frequency shifted using additional modulation of the same order as ν_{FSR} . In particular, the ADF4350 chip with a fractional PLL loop is used, and it can generate frequencies ranging from just below ν_{FSR} to almost double this value, allowing for a great tunable range for a single resonance peak. Since the peaks are spaced by ν_{FSR} , it is possible to lock an arbitrary frequency. The reference shift frequency f_{shift} is thus generated using a PLL, similiar to the one in Fig. 1.1. The CP signal leaving the phase detector is additionally injected with the slower f_{LO} frequency, which results in the two modulations being superposed. The ADF4350 chip itself is controlled from RedPitaya using the SPI protocol.

The remaining RedPitaya connections include connecting the PD signals as inputs, as well as connecting a piezo driver and amplifier to one of the outputs. Remote control of the board is done over an Ethernet cable and the local network, which is also the connection used for sending commands to the to-be-locked laser. The FPGA is programmed with a design that creates f_{LO} from the internal clock and outputs it to the required pins as well as to mixers used in two I/Q demodulator circuits. The demodulated signal is then sent to PID controllers, which manage the piezo output and the signals sent to the Toptica laser. Using the oscilloscope module, the phase shift of both I/Q demodulators is adjusted so that all error signals are visible in the in-phase component alone. Thus, the whole circuit can be simplified to the one visible in Fig. 3.3.

All parameters are controlled programmatically and adjusted for the best PDH operation. Together with a GUI and control of the reference shift, stabilizing the laser frequency, as well as tuning it is a seamless and robust process. The cavity maintains the locked state for days, thanks to the aforementioned protections and the vacuum surrounding it.

3.5. Bandwidth and autocorrelation verification

The conversion scheme was once again set up using the TRA board and optimized for maximal efficiency. Afterwards, the high-precision wavelength meter was turned on and the appropriate

frequency was selected, based on the measured reference frequency and the target difference of 130,726 GHz. Using the frequency lock GUI, the reference was shifted to have its PDH error signal resonances at the same position as the tunable laser. Then, the cavity length, and subsequently the tunable laser frequency, were locked. From now on, tuning occured using just the reference shift and it was adjusted so that the wavelength measured by the wavelength meter matched the target one. Approximately 45 mW of power from each laser was sent to the fiber coupler connected to the photomixer, and a voltage was applied to its electrodes. After some small trial and error tuning, the signal from the single-photon detector began to increase, confirming that the mmWave generation was successful. In contrast to the previous attempt, the conversion was now stable and much stronger; however, it was still orders of magnitude weaker than in the TRA case.

The PCA based generation scheme is a nonlinear process, meaning that in CW mode it is very inefficient. Even with such strong laser beam intensities that were later increased even more as a test, the mmWave signal was not strong enough to observe and measure A-T splitting. Fortunately, it was still possible to measure the bandwidth, as it was simple to detune the mmWave frequency. The measurement was repeated and the result is visualized in Fig. 3.5. The FWHM value was approximately 9 MHz proving that the TRA generated mmWave signal had significant spectral noise that influenced the results.

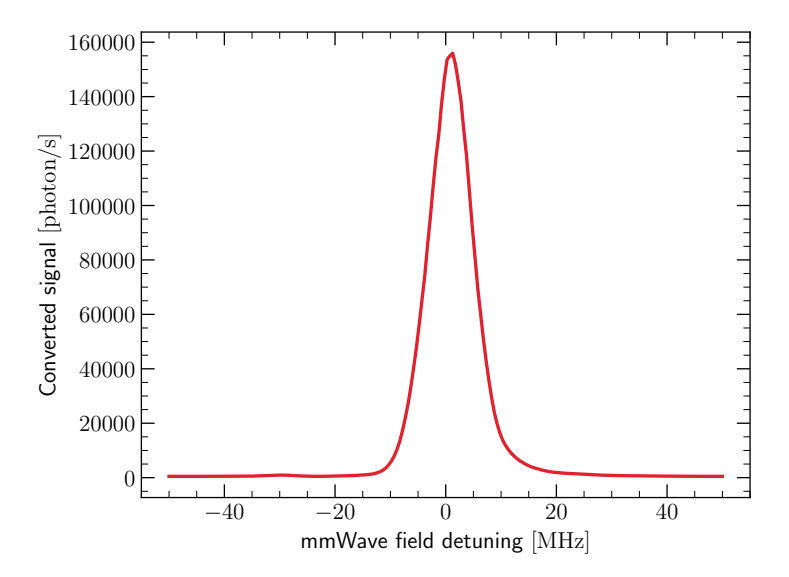


Figure 3.5: Measured photon counts for a range of mmWave frequencies around the resonance. The photomixer output frequency was controlled by tuning one of the constituent lasers using reference shifting. The output mmWave frequency was then calculated using known reference laser wavelength and the applied EOM shifting frequency. The values on the x-axis are the mmWave field detunings from the resonant value obtained using the ARC library.

With the new setup, the overnight autocorrelation measurement was repeated as well, so that it is carried out under conditions similar to those of the bandwidth one. The theoretical value arising from Eq. (2.1-2.2) was recalculated using the new data, which together gave the results displayed in Fig. 3.6. This time the Wiener-Khinchin theory accurately predicted the autocorrelation of thermal photons, proving that the TRA setup was indeed defunct and could not be used to perform further precise measurements.

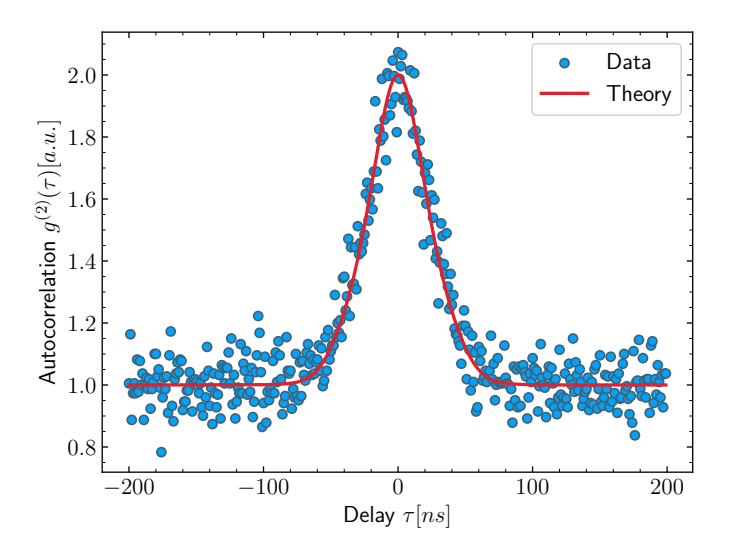


Figure 3.6: Measured autocorrelation of thermal photons. The time delays were calculated by the time controller using predefined time bins and the measurement was performed overnight with the photomixer turned off. The theoretical line was obtained using the measured bandwidth from 3.5 and the Wiener-Khinchin theorem.

3.6. Parametrization

Despite the promising results from the previous measurements, the photomixer could not be used for schemes requiring the measurement of the A-T splitting. While some changes to the EIT spectrum could be observed, they were not strong enough to reliably estimate their value based on direct imaging of the probe field transmission spectrum. As such, there was no way to perform parametrization like before and attempts were made to boost the output intensity of the photomixer. The most trivial solution was to simply send more power via the input lasers, but this has shown to offer little improvement. As the photomixing process is non-linear, increasing the power in CW mode offered little improvement, as the energy would be much better translated to output signal when used with highly energetic impulses. Unfortunately, that was not possible, so other avenues had to be investigated, including another TRA design.

3.7. Planned improvements

Several parts of the setup had a proof of concept approach and were built using components that could be found in the lab, so as to test various ideas before fully committing to the final design. What is more, they were implemented for the TRA board, which had a significant signal output that could saturate the single photon detector, even after transmission through dielectric mirrors or after several partial reflections from the set of polarizers, where a significant part of the signal was transmitted and lost. Now that the photomixer was in place, conserving the signal strength became vital and several ideas were put forth and realized using new equipment.

3.7.1. Parabolic mirror

The most basic setup, without any attenuators in place, involved the mmWave source, a collimating lens and a reflective metallic plate with a drilled hole for optical signals. Metals are very good at reflecting mmWaves, but there was also the issue of the beam waist being much higher than for the laser beams and even the atomic vapour cell itself. The waist of the optical signals was 250 μm , while the mmWave collimated beam was about 2 cm. This problem was solved by ordering a Thorlabs off-axis parabolic mirror with golden coating and a hole parallel to the focused beam. This type of mirror has the advantage of not only reflecting, but also focusing the beam and is used extensively in THz setups. Not only did this improve the coupling of the mmWave electric field with the Rydberg atoms, but it also allowed for using a smaller atomic vapor cell.

3.7.2. Metamaterials

Another improvement was made to the attenuator setup. While it was not really used with the photomixer, its development and conceptualization highlighted the lack of sufficient equipment for handling the polarization of the mmWave field. Crucially, the transitions exploited in the experiment rely on circular polarization of specific handedness, as they offer a much higher dipole moment. The off-the-shelf waveplates available for the THz or mmWave band is very expensive, so another approach was tested first. In particular, a commercially available type of 3D printer filament, high impact polystyrene (HIPS), had been shown to have a refractive index n = 1.5 for the band under consideration [27] and an absorption coefficient is approximately $\alpha = 0.15cm^{-1}$. An initial print of a new collimating lens was therefore performed, as both the TRA radar, as well as the photomixer, were propagating through a TPX glass lens with a focal length of 10 mm. However, it was relatively small and the beam started to spread after around 1m. A larger diameter and focal length were preferred, so as to create a beam with a waist of 2". Therefore, efforts were made to create a better lens and test the possibility of using HIPS elements.

The lens has proven to work as expected and the refractive index and absorption coefficients were experimentally verified to be accurate. This was promising and offered a new direction that would greatly simplify the setup, which is the design of waveplates for polarization control. It would allow not only for more reliable continuous attenuation mechanism, but also for enforcing a proper circular polarization. The mmWave wavelngths are large enough to undergo diffraction on structures that are not too small to be created on a 3D printer. This opens up a world of possibilities as waveplate properties can be created from a metamaterial structure [28, 29, 30]. The use of finite difference time domain (FDTD) simulations would allow for designing such structures that could be later produced directly in the lab.

3.7.3. New electronic design

The last, and probably the most promising solution would be to redesign the TRA board, so as to function correctly and emit a narrowband frequency, free of sidebands that significantly malformed the initial measurements. Such a development would also benefit from the other proposed measures, especially the metamaterial waveplate-based attenuation. The loop filter

capacitor and resistor values need to be meticulously calculated to properly handle noise present in the driving voltages.

Summary

This thesis is an exploration of extending a microwave-to-optical conversion process into the millimeter-wave (mmWave) regime using room-temperature Rydberg atoms. A focal point of the study was the adaptation and refinement of existing microwave conversion technologies to facilitate a precise study of mmWave-to-optical conversion, leveraging the unique properties of Rydberg atoms, with the goal of enabling new measurement methods.

The project initially investigated two primary approaches of mmWave synthesis: employing an automotive radar chip for direct on-chip mmWave generation and utilizing a photomixer for generating mmWaves from optical frequencies. Although the radar chip facilitated successful conversion, challenges related to frequency stability and sideband noise necessitated further exploration and optimization. This led to a more focused investigation on photomixing technologies, which, while less mature in terms of development for continuous wave applications, provided a promising alternative for achieving stable mmWave generation.

Significant achievements of this research included the successful generation and conversion of mmWave frequencies using Rydberg atoms. Through an iterative process of testing the technical limits of the setup, several challenges associated with electronic mmWave frequency synthesis were identified, together with potential mitigation strategies. Accompanying it is the exploration and initial testing of a photomixer setup, which, despite its lower power output, proved sufficient to carry out basic measurements and verify the results obtained using the radar chip.

The outcomes of this thesis pave the way to future work with the mmWave frequency band, with the Rydberg atom converter proving its capability of transducing such photons to optical ones. Future work will focus on enhancing the efficiency and stability of these generation processes, integrating novel photonic devices, and refining the control mechanisms to better harness the properties of Rydberg atoms for practical and scalable quantum technologies.

References

- [1] Sebastian Borówka, Uliana Pylypenko, Mateusz Mazelanik, and Michał Parniak. Continuous wideband microwave-to-optical converter based on room-temperature Rydberg atoms. *Nature Photonics*, 18(1):32–38, January 2024.
- [2] Kevin K. S. Multani, Hubert Stokowski, Emma Snively, Rishi Patel, Wentao Jiang, Nathan Lee, Paul B. Welander, Emilio A. Nanni, and Amir H. Safavi-Naeini. Development of a millimeter-wave transducer for quantum networks. In 2020 45th International Conference on Infrared, Millimeter, and Terahertz Waves (IRMMW-THz), pages 1–2, 2020.
- [3] Hubert Stokowski, Marek Pechal, Emma Snively, Kevin Multani, Paul Welander, Jeremy Witmer, Emilio Nanni, and Amir Safavi-Naeini. Towards millimeter-wave based quantum networks. pages 1–2, 09 2019.
- [4] H. Wu, R. Richaud, J.-M. Raimond, M. Brune, and S. Gleyzes. Millisecond-lived circular rydberg atoms in a room-temperature experiment. *Phys. Rev. Lett.*, 130:023202, Jan 2023.
- [5] Jinpeng Yuan, Wenguang Yang, Mingyong Jing, Hao Zhang, Yuechun Jiao, Weibin Li, Linjie Zhang, Liantuan Xiao, and Suotang Jia. Quantum sensing of microwave electric fields based on rydberg atoms. Reports on Progress in Physics, 86(10):106001, September 2023.
- [6] Hao Zhang, Yu Ma, Kaiyu Liao, Wenguang Yang, Zongkai Liu, Dongsheng Ding, Hui Yan, Wenhui Li, and Linjie Zhang. Rydberg atom electric field sensing for metrology, communication and hybrid quantum systems. *Science Bulletin*, March 2024.
- [7] Christopher L. Holloway, Joshua A. Gordon, Andrew Schwarzkopf, David A. Anderson, Stephanie A. Miller, Nithiwadee Thaicharoen, and Georg Raithel. Sub-wavelength imaging and field mapping via electromagnetically induced transparency and autler-townes splitting in rydberg atoms. *Applied Physics Letters*, 104(24):244102, June 2014.
- [8] Matthew T. Simons, Abdulaziz H. Haddab, Joshua A. Gordon, and Christopher L. Holloway. A rydberg atom-based mixer: Measuring the phase of a radio frequency wave. *Applied Physics Letters*, 114(11):114101, March 2019.
- [9] Joshua A. Gordon, Matthew T. Simons, Abdulaziz H. Haddab, and Christopher L. Holloway. Weak electric-field detection with sub-1 hz resolution at radio frequencies using a rydberg atom-based mixer. AIP Advances, 9(4):045030, April 2019.

- [10] Mingyong Jing, Ying Hu, Jie Ma, Hao Zhang, Linjie Zhang, Liantuan Xiao, and Suotang Jia. Atomic superheterodyne receiver based on microwave-dressed rydberg spectroscopy. *Nature Physics*, 16(9):911–915, June 2020.
- [11] Joshua A. Gordon, Christopher L. Holloway, Andrew Schwarzkopf, Dave A. Anderson, Stephanie Miller, Nithiwadee Thaicharoen, and Georg Raithel. Millimeter wave detection via autler-townes splitting in rubidium rydberg atoms. *Applied Physics Letters*, 105(2):024104, July 2014.
- [12] Gianluca Allinson, Matthew J. Jamieson, Lucy Downes, Andrew R. Mackellar, C. Stuart Adams, and Kevin J. Weatherill. Simultaneous multi-band radio-frequency detection using high-orbital-angular-momentum states in a rydberg-atom receiver, 2023.
- [13] N. Šibalić, J.D. Pritchard, C.S. Adams, and K.J. Weatherill. Arc: An open-source library for calculating properties of alkali rydberg atoms. *Computer Physics Communications*, 220:319–331, 2017.
- [14] Analog Devices, Inc. Fundamentals of Phase Locked Loops (PLLs), 2009.
- [15] Ran Finkelstein, Samir Bali, Ofer Firstenberg, and Irina Novikova. A practical guide to electromagnetically induced transparency in atomic vapor. *New Journal of Physics*, 25(3):035001, mar 2023.
- [16] A. K. Mohapatra, T. R. Jackson, and C. S. Adams. Coherent optical detection of highly excited rydberg states using electromagnetically induced transparency. *Phys. Rev. Lett.*, 98:113003, Mar 2007.
- [17] H. Kübler, J. P. Shaffer, T. Baluktsian, R. Löw, and T. Pfau. Coherent excitation of rydberg atoms in micrometre-sized atomic vapour cells. *Nature Photonics*, 4(2):112–116, Feb 2010.
- [18] Sebastian Borówka, Uliana Pylypenko, Mateusz Mazelanik, and Michał Parniak. Sensitivity of a rydberg-atom receiver to frequency and amplitude modulation of microwaves. *Appl. Opt.*, 61(29):8806–8812, Oct 2022.
- [19] Sebastian Borówka, Mateusz Mazelanik, Wojciech Wasilewski, and Michał Parniak. Optically-biased rydberg microwave receiver enabled by hybrid nonlinear interferometry, 2024.
- [20] Phase and Frequency of Laser Light | TOPTICA Photonics AG toptica.com. https://www.toptica.com/application-notes/phase-and-frequency-locking-of-diode-lasers/phase-and-frequency-of-laser-light. [Accessed 25-04-2024].
- [21] R. W. P. Drever, J. L. Hall, F. V. Kowalski, J. Hough, G. M. Ford, A. J. Munley, and H. Ward. Laser phase and frequency stabilization using an optical resonator. *Applied Physics B Photophysics and Laser Chemistry*, 31(2):97–105, June 1983.
- [22] Eric D. Black. An introduction to pound–drever–hall laser frequency stabilization. *American Journal of Physics*, 69(1):79–87, January 2001.
- [23] C. E. Liekhus-Schmaltz, R. Mantifel, M. Torabifard, I. B. Burgess, and J. D. D. Martin. Injection-locked diode laser current modulation for pound-drever-hall frequency stabilization using transfer cavities. *J. Opt. Soc. Am. B*, 29(6):1394–1398, Jun 2012.

- [24] Kondephy. Pound-Drever-Hall scheme, distributed under CC 4.0 license, 2016. File: https://commons.wikimedia.org/w/index.php?lang=en&title=File%3APound% E2%80%93Drever%E2%80%93Hall_technique.svg.
- [25] Anthony E. Siegman. Lasers. University Science Books, 1986.
- [26] lodewyck. GaussianBeam sourceforge.net. https://sourceforge.net/projects/gaussianbeam/. [Accessed 13-05-2024].
- [27] C. Harrison Brodie, Isaac Spotts, Hajer Reguigui, Camille A. Leclerc, Michael E. Mitchell, Jonathan F. Holzman, and Christopher M. Collier. Comprehensive study of 3d printing materials over the terahertz regime: absorption coefficient and refractive index characterizations. *Optical Materials Express*, 12(9):3379, August 2022.
- [28] A. I. Hernandez-Serrano, Qiushuo Sun, Elizabeth G. Bishop, Elliott R. Griffiths, Christopher P. Purssell, Simon J. Leigh, J. Lloyd-Hughes, and Emma Pickwell-MacPherson. Design and fabrication of 3-d printed conductive polymer structures for thz polarization control. Optics Express, 27(8):11635, April 2019.
- [29] David Rohrbach, Bong Joo Kang, and Thomas Feurer. 3d-printed thz wave- and phase-plates. *Optics Express*, 29(17):27160, August 2021.
- [30] Alexander Jäckel, David Ulm, Thomas Kleine-Ostmann, Enrique Castro-Camus, Martin Koch, and Jan Ornik. Achromatic quarter-waveplate for the terahertz frequency range made by 3d printing. *Journal of Infrared, Millimeter, and Terahertz Waves*, 43(7–8):573–581, August 2022.